Accelerating CO_2 Electroreduction to Multi-carbon Products via Synergistic Electric-thermal Field on Copper Nanoneedles

Baopeng Yang[1, $], Kang Liu[1, $], HuangJingWei Li[1, $], Changxu Liu[2, $], Junwei Fu[1], Hongmei Li[1], Jianan Erick Huang[3], Pengfei Ou[3], Tartela Alkayyali[4], Chao Cai[1], Yuxia Duan[1], Hui Liu[5], Pengda An[6], Ning Zhang[6], Wenzhang Li[7], Xiaoqing Qiu[7], Chuankun Jia[8], Junhua Hu[9], Liyuan Chai[5], Zhang Lin[5], Yongli Gao[10], Masahiro Miyauchi[11], Emiliano Cortés[2], and Stefan A. Maier[2,12, *], Min Liu[1, *]

[1] Hunan Joint International Research Center for Carbon Dioxide Resource Utilization, State Key Laboratory of Powder Metallurgy, School of Physical and Electronics, Central South University, Changsha 410083, China.

[2] Chair in Hybrid Nanosystems, Nanoinstitute Munich, Faculty of Physics, Ludwig-Maximilians-Universität München, D-80539 München, Germany.

[3] Department of Electrical and Computer Engineering, University of Toronto, Toronto, Ontario M5S 1A4, Canada.

[4] Department of Mechanical and Industrial Engineering, University of Toronto, Toronto, Ontario M5S 3G8, Canada.

[5] School of Metallurgy and Environment, Central South University, Changsha 410083, China.

[6] School of Materials Science and Engineering, Central South University, Changsha 410083, China.

[7] School of Chemistry and Chemical Engineering, Central South University, Changsha 410083, China.

[8] College of Materials Science and Engineering, Changsha University of Science & Technology, Changsha 410114, China.

[9] School of Materials Science and Engineering, Zhengzhou University, Zhengzhou 450002, China.

[10] Department of Physics and Astronomy, University of Rochester, Rochester, NY, 14627, USA.

[11] Department of Materials Science and Engineering, School of Materials and Chemical Technology, Tokyo Institute of Technology, Tokyo 152-8552, Japan.

[12] Department of Physics, Imperial College London, London SW7 2AZ, UK.

[$] These authors contributed equally: Baopeng Yang, Kang Liu, HuangJingWei Li, Changxu Liu.

*e-mail: Stefan.Maier@physik.uni-muenchen.de; minliu@csu.edu.cn.

Abstract

Electrochemical CO_2 reduction is a promising way to mitigate CO_2 emissions and close the anthropogenic carbon cycle. Among products from CO_2RR, multi-carbon chemicals, such as ethylene and ethanol with high energy density, are more valuable. However, the selectivity and reaction rate of C_2 production are unsatisfactory due to the sluggish thermodynamics and kinetics of C–C coupling. Electric field and thermal field have been studied and utilized to promote catalytic reactions as they can regulate the thermodynamic and kinetic barriers of reactions. Either raising the potential or heating the electrolyte can enhance C–C coupling, but these come at the cost of increasing side reactions, such as hydrogen evolution reaction. Here, we present a generic strategy to enhance local electric field and temperature simultaneously, dramatically improve the electric-thermal synergy desired in electrocatalysis. A conformal coating of ~5-nm polytetrafluoroethylene significantly improves the catalytic ability of copper nanoneedles (~7 fold electric field and ~40 K temperature enhancement at tips compared with bare copper nanoneedles experimentally), resulting in an improved C2 Faradaic efficiency of over 86% at a partial current density of more than 250 mA cm^{-2} and an record-high C2 turnover frequency of 11.5±0.3 s^{-1} Cu $site^{-1}$. Combined with its low cost and scalability, the electric-thermal strategy for state-of-art catalyst not only offers a new insight to improve activity and selectivity of value-added C_2 products as we demonstrated, but also inspires advances in efficiency and/or selectivity of other valuable electro-/photo-catalysis such as hydrogen evolution, nitrogen reduction and hydrogen peroxide electrosynthesis.

INTRODUCTION

Electrochemical conversion of carbon dioxide (CO_2) into value-added carbon-based feedstocks and fuels by utilizing the renewable electricity is a promising technology to mitigate CO_2 emissions, fulfil the anthropogenic carbon cycle and store the excess renewable electricity as chemical energy.[1–3] Among various products produced from CO_2 reduction reaction (CO_2RR), two-carbon (C_2) hydrocarbons and oxygenates, such as ethylene (C_2H_4) and ethanol (EtOH), are attractive in view of their high energy densities and major roles in chemical industry.[1,2] However, the selectivity and reaction rate for C_2 productions are still below the demands for practical applications, due to the sluggish thermodynamics and kinetics of C–C coupling.[4–8]

Raising the coverage of *CO, a key intermediate for C–C coupling,[4,5,8] and simultaneously lowering the energy barrier of *CO dimerization on catalyst would effectively improve C–C coupling.[9–19] Although many efforts have been tried to implement these by regulating the electronic properties of Cu, such as elements doping,[9–11] facets controlling,[12,13] heterojunction interface constructing,[14–16] and defects creating,[17–19] the complexity and finiteness of electronic structure tuning impede their application at scale.

Electric field has been extensively studied and utilized to improve the activity and selectivity of catalytic reactions as it can accumulate reactants and regulate the thermodynamic barriers of reactions.[20–27] Similar to electric field, thermal field can promote the reaction rate through facilitating kinetic process.[28–32] Therefore, introducing the electric field and thermal field (denote as electric-thermal field) synchronously on Cu surface would be an effective way to improve the selectivity and reaction rate of C_2 products during CO_2RR. A simple way to enhance electric-thermal field is directly raising the applied potential and heating the electrolyte. However, it comes at the cost of increasing hydrogen evolution reaction (HER) and the generation of C_1, because the HER and C_1 production are more likely to be activated than that of C2 production.[20,25,31,33]

In this work, we report a synergetic electric-thermal field strategy, by conformal coating Cu nanoneedle (Cu NN) bodies with polytetrafluoroethylene (PTFE) to produce a locally enhanced local electric-thermal field at tips, to raise *CO intermediates and facilitate C–C coupling for high-efficiency conversion of CO_2 to C_2 products. Finite element method (FEM) simulations show that Cu NN tip possesses a local electric-thermal field and this electric-thermal field can be further enhanced by pushing electrons to the top tip through covering Cu NN body with dielectric polymer. Density functional theory (DFT) calculations indicate the enhanced electric field lowers the Gibbs free energy (ΔG) of C–C coupling, and the enhanced thermal field boosts the reaction rate of C–C coupling. Inspired by these aspects, we synthesize a series of Cu NNs with different PTFE coverage (Cu-PTFE NNs) and verify the electric-thermal field at tips through the adsorbed K^+ concentration and infrared thermal imaging tests, which show about 3-fold enhancement with the increase of PTFE coverage. *In-situ* Fourier transform infrared (FTIR) investigations confirm the *CO accumulation and C–C coupling acceleration. As a result, we implement a conversion of CO_2 to C_2 with a Faradaic efficiency (FE) of over 86% and a half-cell cathodic energy efficiency (CEE) of ~50% at a partial current density of over 250 mA cm^{-2}, and a record-high turnover frequency (TOF) of 11.5±0.3 s^{-1} Cu $site^{-1}$ to the best of our knowledge. This work opens a new avenue to improve the selectivity and activity of Cu-based catalysts. More importantly, the conformal coating may be transferred to other catalytic platforms demanding synergic effect of improved electric field and temperature at nanoscale.

RESULTS AND DISCUSSION

FEM simulations and DFT calculations. High-curvature metallic structures are known to accumulate electrons, spontaneously increase local electron density and collision, leading to a locally enhanced electric field and high temperature (thermal field) at the tip (Fig. S1a).[20,23,34–37] We speculate that the tip-induced electric field and thermal field (defined as electric-thermal

field) can be further enhanced by covering dielectric polymer on needle body to concentrate electrons on the very top point of a tip (Fig. S1b). To verify this assumption, we employed FEM simulations to investigate the distribution of electron density, electric field, and thermal field on the tip of Cu NN with different PTFE coverage rates. We found that with the PTFE coverage rates increasing from 0% to 99%, the tip-concentrated electron density showed 2-fold enhancement (Figs. S2 and S3), resulting in an obviously enhanced electric field and thermal-field at the tips (Fig. 1a, b and Figs. S4, S5). Remarkably, the tip-induced electric field and thermal field showed a sharp enhancement as PTFE coverage increased, and achieved about 2-fold (from 26.3×10^3 to 50.3×10^3 kV m^{-1}) and 3-fold (from 17 to 62 K) enhancement, respectively (Fig. 1c and Table. S1). In contrast to sharp-tip Cu NN, the electric field and thermal field enhancements are negligible for quasi-planar Cu nanoparticle (Cu NP) (Figs. S6, S7 and Table S1). We also investigated the relationship between electric-thermal field and applied bias (Fig. S8), the results showed that the tip-induced electric field and thermal field showed an enhancement as applied bias increased.

To explore how the tip-induced electric-thermal field influence the C_2 formation, DFT calculations were applied to survey the *CO dimerization process on Cu surface, which is the key rate-limiting step along the CO_2-to-C_2 pathway.[38,39] We introduced various electric fields onto Cu(100) surface, a facet that has been confirmed to favor C_2 formation,[40–42] and used an explicit water model[43] to calculate the thermodynamic energy barriers for *CO dimerization (Fig. 1d and Table S2). We found that the ΔG of *CO dimerization decreased with the electric field increasing, suggesting that the electric field is thermodynamically favorable for C_2 formation. In order to study the kinetics process of *CO dimerization, we then calculated the activation energy (ΔE_a) and TOF of *CO dimerization *via*:[44]

$$TOF = \frac{kT}{h} \times exp(-\frac{\Delta E_a}{kT})$$

where k is the Boltzmann constant, h is Planck's constant, T is temperature in Kelvins, and ΔE_a is the calculated activation energy of *CO dimerization. Similar to ΔG, ΔE_a decreased with the increase of electric field, indicating that the electric field also favors C_2 generation kinetically (Figs. S9, S10 and Table S2). A TOF map of *CO dimerization at various electric field and thermal field shows that the TOF grows more than two orders of magnitude with the increase of the electric field and thermal field (Fig. 1e). Obviously, the thermal field vastly improves the kinetics process of *CO dimerization (Fig. S11). These findings predict that locally enhanced electric-thermal field accelerates *CO dimerization both thermodynamically and kinetically (Fig. 1f).

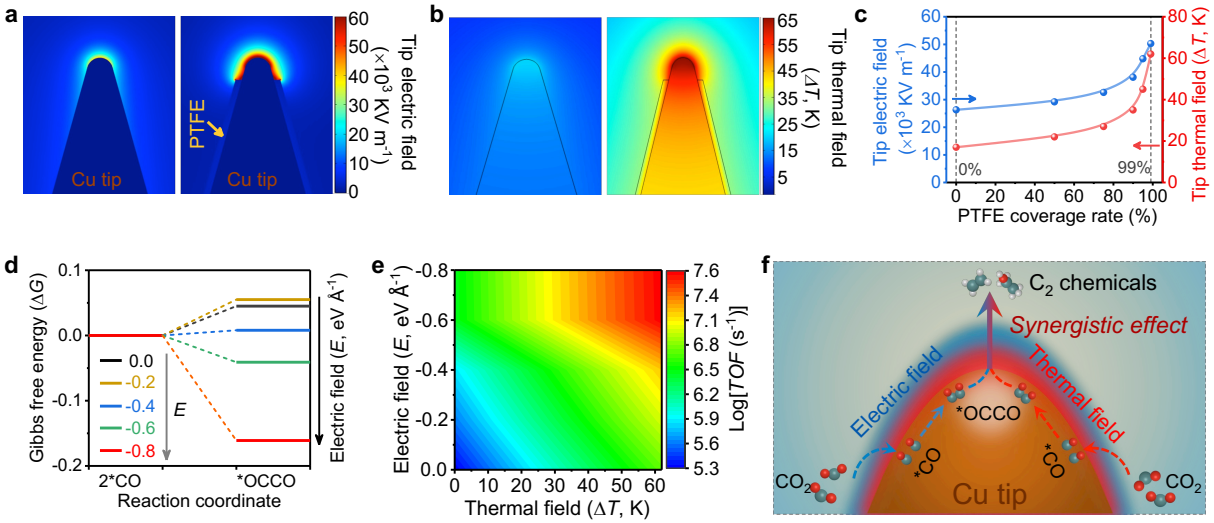

Figure 1. FEM simulations and DFT calculations. a, The electric field distribution on a pristine Cu NN (left) and a Cu NN with 99% PTFE coverage (right). **b,** The thermal field distribution on a pristine Cu NN (left) and a Cu NN with 99% PTFE coverage (right). The thermal field (ΔT, K) is the temperature enhancement versus room temperature (298 K). **c**, The electric field and thermal field at Cu NN tips as a function of PTFE coverage rates. **d**, Reaction Gibbs free energy diagrams of *CO dimerization to form *OCCO on Cu(100) surface under different electric fields. **e**, A TOF map of *CO dimerization on Cu(100) under various electric field and thermal field. **f**, A schematic illustration of the synergetic effect of tip-induced electric field and thermal field on promoting C_2 formation.

Catalyst synthesis and characterization. To probe our predictions experimentally, we prepared a suite of Cu NNs with PTFE coverage rates from 0 to 99% (Fig. S12 and Table S3). Scanning electron microscopy (SEM) images reveal the obtained Cu samples have needle morphologies and visible PTFE layers on needle bodies (Fig. S13). Transmission electron microscopy (TEM), high-angle annular dark-field scanning TEM (HAADF-STEM), and energy-dispersive X-ray spectroscopy (EDX) elemental mapping analyses confirm the well PTFE coverage on Cu NN bodies and only the top tip exposed (Fig. 2 and Fig. S14).

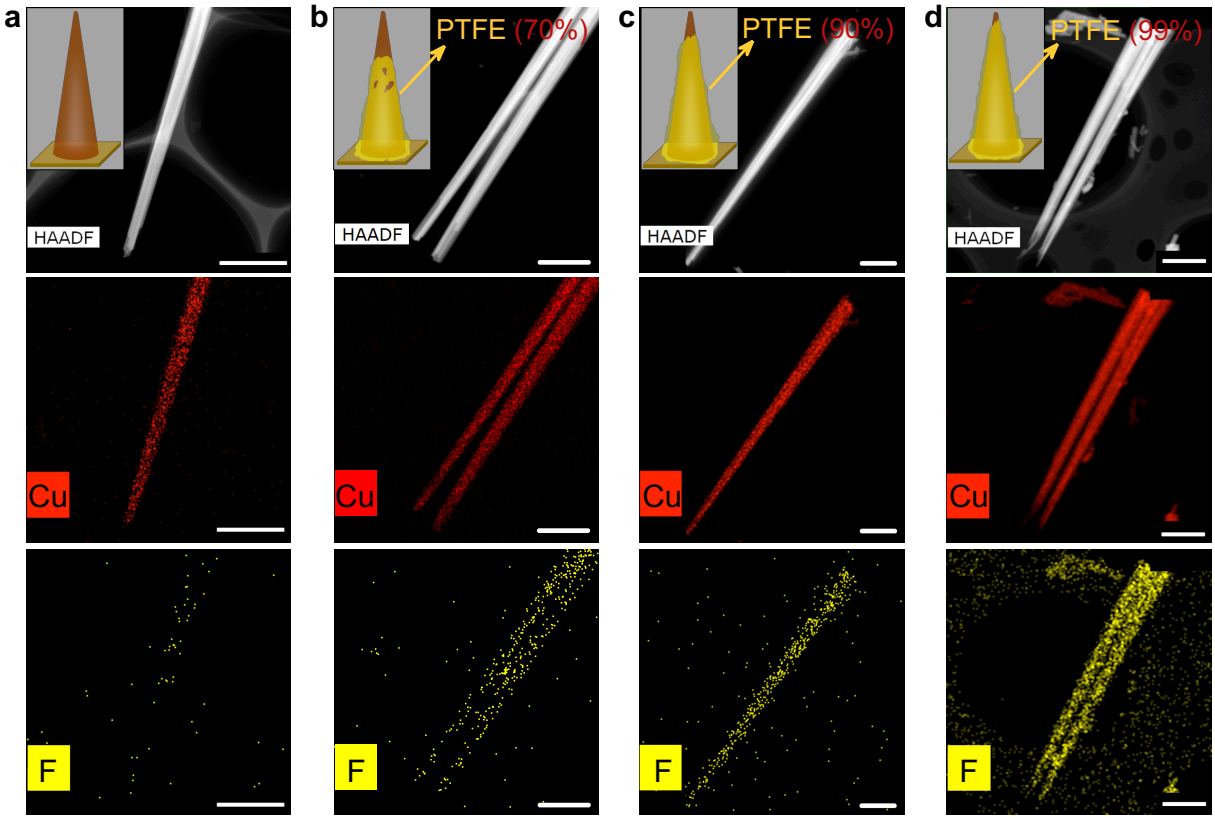

Figure 2. Structural characterization. a-d, HAADF-STEM images and the corresponding elemental mapping of Cu (red) and F (yellow) taken from a section of (**a**) pristine Cu NN, (**b**) Cu NN with a PTFE coverage rate of 70% (Cu-PTFE-70 NN), (**c**) Cu NN with a PTFE coverage rate of 90% (Cu-PTFE-90 NN), and (**d**) Cu NN with a PTFE coverage rate of 99% (Cu-PTFE-99 NN). Scale bars, 1 μm. Insets: schematic illustrations of the coverage status of PTFE on Cu NN bodies. PTFE coverage rates were estimated from SEM and TEM analyses.

To determine the morphological structure and chemical state of the tested catalysts, SEM and a series of spectroscopies were performed. Before CO_2RR test, all catalysts were operated under a constant voltage of –1.4 V versus reversible hydrogen electrode (vs. RHE) until the current was stable (Fig. S15). SEM and EDX mapping images reveal that the catalysts retain the needle structure with well PTFE coverage after electroreduction (Figs. S16 and S17). FTIR spectra of Cu-PTFE NNs before and after electroreduction show two visible characteristic peaks of PTFE located at 1100–1300 cm^{-1} (Fig. S18),[45] confirming the coverage of PTFE. X-ray diffraction (XRD) patterns and X-ray photoelectron spectroscopy (XPS) spectra (Fig. S19) reveal that the Cu-PTFE NNs are metallic Cu after electroreduction,[46] which is further confirmed by the Cu K edge X-ray absorption near-edge spectra (XANES) and the extended X-ray absorption fine structure (XAFS) (Fig. S20).[11,46]

The effect of tip-induced electric-thermal field. To probe the enhanced electric field at the tips, we measured the concentration of adsorbed K^+ on electrodes. The results show that Cu NN with a sharp tip structure has a higher K^+ concentration than that of quasi-planar Cu NP, and the adsorbed K^+ concentration can be further enhanced when Cu NN is covered with PTFE (Figs. S21-23 and Table S4). This finding indicates that the electric field of Cu NN can be enhanced to about 7-fold by covering PTFE (Fig. 3a). We then probed the local thermal field by using an infrared thermal camera system. The temperature distribution on a single Cu needle electrode (Fig. S24) shows a high temperature near the tip, indicating that the sharp tip can produce a local thermal field due to electron collision. Compared with planar Cu NP, the pristine Cu NN shows about 4-fold higher temperature increment, and the temperature increment can be further enhanced to nearly 14-fold for Cu-PTFE-99 NN (Fig. 3b and Figs. S25 and S26). These results (Figs. 3a and b) indicate that the electric-thermal field at tip can be improved by tuning PTFE coverage, which is consistent with our theoretical simulations.

We then explored the capacity regarding adsorption and activation of CO_2 and CO molecules on Cu-PTFE NNs *via* gas electro-response experiments (Fig. S27). The results (Fig. 3c and Fig. S28) show that the CO_2 and CO adsorption responses become stronger with the increase of PTFE coverage, suggesting that the adsorption and activation of CO_2 and CO are promoted by enhancing the tip-induced electric-thermal field.[9,47]

To further investigate how the tip-induced electric-thermal field modulate the adsorption and dimerization of *CO intermediates, *in-situ* attenuated total reflection FTIR (ATR-FTIR, Fig. S29) was conducted. The spectra show an obvious stretching band of linearly bonded CO (CO_L) in the range of 1950–2150 cm^{-1} (Fig. 3d and Figs. S30-32).[48–53] With the applied potentials stepping down from –0.2 to –0.9 V vs. RHE, CO_L stretching band areas increase gradually, indicating the *CO amount increased with the electric field (Fig. 3e). Then, with the negative shift of the potential from –0.9 V to –1.5 V, CO_L stretching band areas decreased with an accelerated rate as the PTFE coverage increased, indicating that the abundant *CO intermediates were consumed quickly to implement a fast *CO dimerization process under the enhanced thermal field (Fig. S33, the details see supporting information).[49,51] The time-resolved *in-situ* ATR-FTIR spectra at the potential of –0.9 and –1.5 V vs. RHE (Figs. S34 and S35) confirmed that the *CO formation and dimerization process were accelerated by increasing the electric field and thermal field, respectively. These findings demonstrate that the local electric-thermal field can enrich *CO intermediates on active sites and accelerate *CO dimerization to produce C_2 products.

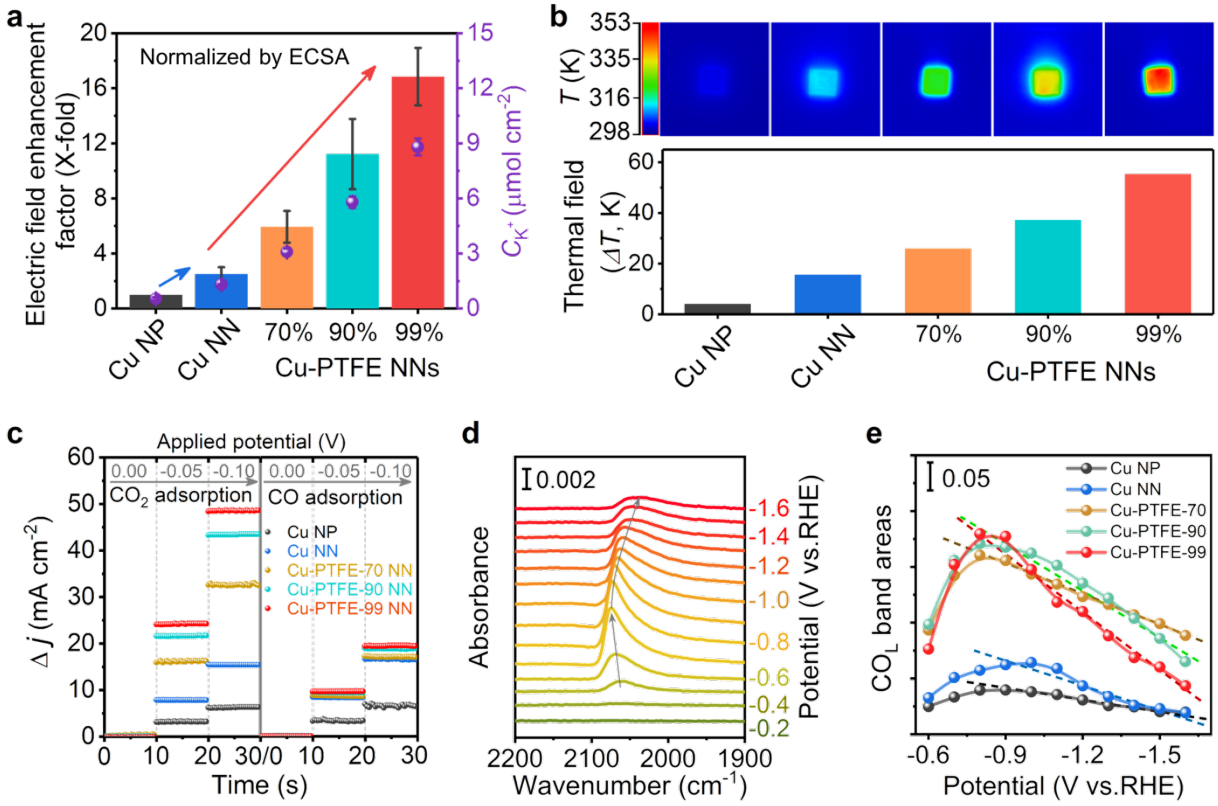

Figure 3. Electric-thermal field detection and enhancement mechanism investigation. a, The electric field enhancement factor and the concentration of adsorbed K^+ ions on the surface of electrodes at a potential of –1.5V vs. RHE, normalized by ECSA. Error bars correspond to the standard deviation of three independent electrode measurements. The electric field enhancement factor was estimated from the adsorbed K^+ concentrations by using Cu NP as reference. **b**, Infrared thermal imaging of the electrodes (top) and corresponding thermal field magnitude (bottom) at an applied constant current. **c**, The results of CO_2 (left) and CO (right) adsorption responses under different applied voltages. **d**, *In-situ* ATR-FTIR spectra of Cu-PTFE-99 NN electrode under different potentials. **e**, The stretching band areas of atop-bound CO_L in the 1950–2150 cm^{-1} range as a function of potentials.

Electrochemical CO_2 reduction performance. To validate the enhancement of CO_2RR by tip-induced electric-thermal field, we evaluated the CO_2RR performance of these catalysts in a conventional H-cell with CO_2-saturated 0.1 M $KHCO_3$ electrolyte (pH 6.8). We detected and

analyzed the products under different potentials (Fig. S36 and Table S5) through gas chromatography (GC) and nuclear magnetic resonance (NMR). The product distributions under a potential of –1.5 V vs. RHE (Fig. 4a) show that the main product for all Cu NN electrodes is C_2, whereas C_1 account for the majority products on Cu NP electrode. The FE of C_2 for pristine Cu NN was 43.1±1.9% at –1.5 V vs. RHE, much higher than that of 21.2±1.7% for Cu NP. This value can be further enhanced with the increase of PTFE coverage rate. And a C_2 FE of 86.1±2.2% was obtained on the very top tip exposed Cu-PTFE-99 NN electrode (Fig. 4b). This trend was retained even under a wide potential range (Fig. S37 and Table S5), confirming that the tip-induced local electric-thermal field enhancement are favorable for C_2 generation versus C_1 and H_2 formation during CO_2RR.

To explore the intrinsic activity, we investigated the electrochemical surface areas (ECSAs) and current densities of all electrodes (Figs. S38-42 and Tables S6, S7). ECSAs decreased with the increase of PTFE coverage rate as the active sites on needle body was covered by PTFE. However, the partial current densities of C_2 enhance with PTFE coverage rate increasing, and achieve a 4-fold enhancement for the very top tip exposed Cu-PTFE-99 NN compared with that of pristine Cu NN.

To determine the activity of per active site experimentally, we calculated the TOFs of C_2 production at the potential of –1.5 V vs. RHE (Figs. 4c, S43, S44 and Tables S8, S9). Compared with Cu NP, Cu-PTFE NNs exhibit higher TOFs, which increase with the PTFE coverage and reach a value of 11.5±0.3 s^{-1} Cu $site^{-1}$ at Cu-PTFE-99 NN. This TOF value was about 5 times higher than that of Cu NN (2.7±0.1 s^{-1} Cu $site^{-1}$) and outperformed the reported values, even ones for most single-atom catalysts (Table S10), proving the local electric-thermal field can greatly accelerate the C_2 formation during CO_2RR.

Then, we investigated the CO_2RR performance of Cu NN under different electrolyte temperature. We found that enhancing the electrolyte temperature promotes the CO_2RR, but it

is more favorable for C_1 and H_2 formation versus C_2 formation (Fig. S45). Comparing the results of directly enhancing electrolyte temperature (heating the electrolyte to artificially enhance global temperature, denoted as *Electrolyte temperature*) and locally enhancing tip temperature (applying a potential to spontaneously enhance local temperature at copper nanoneedle tips during CO2RR, denoted as *Tip local temperature*), we found that locally enhancing tip temperature by tuning PTFE coverage rate on Cu NN body is more favourable for C_2 formation because it can directly act on C_2 active sites to accelerate *CO dimerization, rather than on C_1 or H_2 active sites to produce C_1 and H_2 (Fig. S46).

To increase the gas reactant availability at the electrode surface, we also explored the CO_2RR performance in a flow-cell (Fig. S47). We deposited Cu NP, pristine Cu NN and Cu-PTFE-99 NN onto PTFE membrane gas-diffusion electrodes (GDEs) by spray coating and tested their CO_2RR activity in 1 M KOH. Among the samples, Cu-PTFE-99 NN still exhibited the best activity and selectivity for C_2 production (Figs. S48, S49 and Table S11).

Next, we assessed the catalytic activity of Cu-PTFE-99 NN in the current density range of 100−700 mA cm^{-2} (Figs. 4d, S50, S51 and Tables S11, S12). Under all tested current densities, the FEs for C_2 products were measured over 80%, indicating the promising for practical applications. Under the current density of 300 mA cm^{-2}, the best C_2 FE of 85.4±1.5% were achieved with a partial current density of 256.2±4.6 mA cm^{-2} at a low overpotential of –0.77 V vs. RHE. The calculated half-cell CEE of C_2 products was 49.3±2.0% for Cu-PTFE-99 NN (Fig. S52 and Table S12), which approached the reported state-of-the-art catalysts (55% for Cu-Al alloys[10]). The Cu-PTFE-99 NN had a high stability in flow-cell with a total current density of 300 mA cm^{-2} for over 25 h (Fig. 4e). The very top tip exposed Cu-PTFE-99 NN catalyst approached or outperformed the reported state-of-the-art Cu-based catalysts in performance (Table S13), benefitting from the synergistic promoting effect of electric-thermal field.

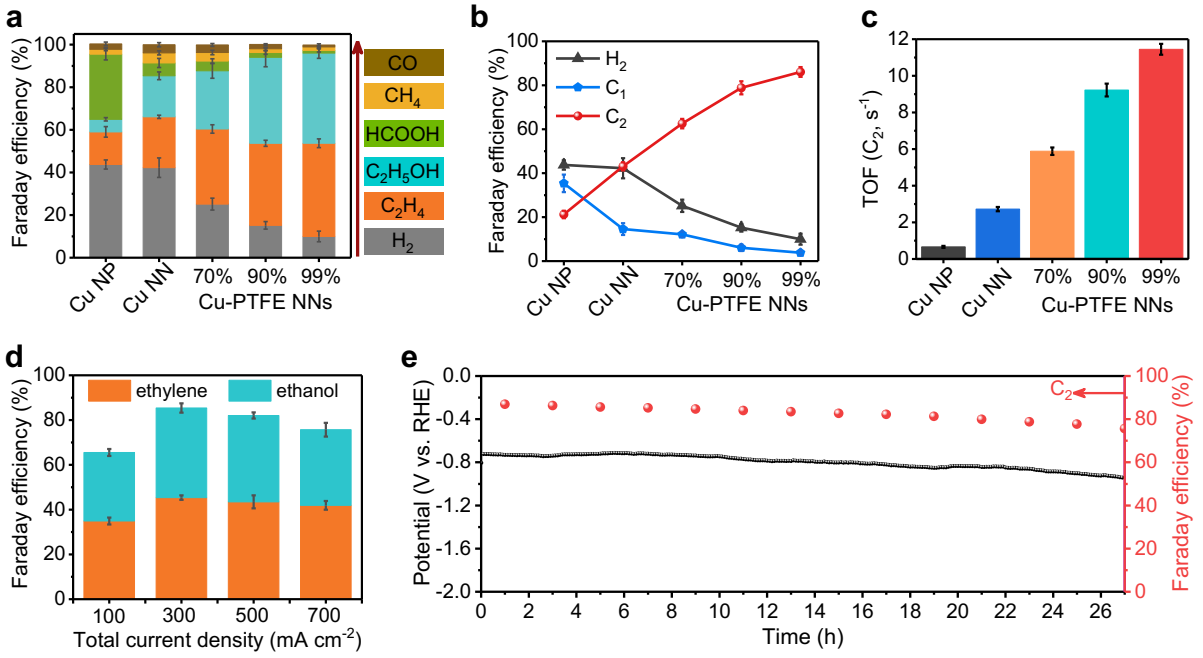

Figure 4. CO_2 electroreduction performance investigation. **a**, Products distribution and corresponding FEs under the potential of –1.5 V vs. RHE in H-cell. **b**, The FEs of C_2, C_1 and H_2 products under the potential of –1.5 V vs. RHE in H-cell. **c**, TOFs under the potential of –1.5 V vs. RHE in H-cell. **d**, FEs of C_2 products on Cu-PTFE-99 NN under different current densities in Flow-cell. **e**, Potential and FEs of C_2 products measured during 27 h of continuous operation at the current density of 300 mA cm^{-2}. Error bars correspond to the standard deviation of three independent electrode measurements.

CONCLUSION

In summary, we developed a strategy to accelerate the conversion of CO_2-to-C_2 by a PTFE conformal coating on Cu NN body to generate a locally enhanced electric-thermal field at tip. Combining the theoretical studies and experimental investigations, we concluded that the electric-thermal field at Cu NN tip can be controllably tuned by adjusting the coverage of PTFE on body, and the locally enhanced electric-thermal field raised *CO intermediates and accelerated C–C coupling both thermodynamically and kinetically. Using this strategy, we achieved a C_2 FE of 85.4±1.5% at a partial current density of more than 250 mA cm^{-2}, and a

high TOF of 11.5±0.3 s^{-1} Cu $site^{-1}$ for C_2 generation. The findings suggest a new strategy for improving CO_2 conversion into value-added C_2 chemicals using renewable electricity with the aid of local electric-thermal field synergy. Considering the ease of fabrication and excellent scalability, we anticipate that this strategy—tuning local electric-thermal field on catalyst surface—may be generalized to promote other electrocatalytic reaction, by virtue of the unparalleled ability to enhancement in electric field and temperature at nanoscale.

EXPERIMENTAL SECTION

COMSOL Multiphysics simulations. In our work, the FEM model was constructed in COMSOL Multiphysics v 5.5 as a stationary, 2D axisymmetric model and consisted of a Cu needle, a PTFE layer, and an electrolyte diffusion layer. Conventional triangular meshes were used for all simulations and the meshes were set to the densest grid around the electrode and PTFE surfaces. The MUMPS solver was used with a relative tolerance of 0.001.

The 'Electric Currents' module was used to solve the electron density and electric field when the electrode is under a specific potential bias. The electric field, *E*, was computed as the negative gradient of the electric potential as follows:

$$E = -\nabla V$$

Additionally, Ohm's law was used to correlate the electric field to current density, *J*, as follows:

$$J = \sigma E$$

in which σ is the electrical conductivity. The electrical conductivity of the copper electrode was set to be 5.998×10^{7} S m^{-1}, while the PTFE layer conductivity and electrolyte conductivity were assumed to be 1×10^{-15} S m^{-1} and 10 S m^{-1}, respectively. The dielectric model was also used to relate the electric displacement, D, with the electric field as follows:

$$D = \varepsilon_0 \varepsilon_r E$$

where ε_0 represents the dielectric constant of vacuum and ε_r represents the dielectric constant of the materials (1 for Cu, 2.1 for PTFE, and 80 for the electrolyte). An electric potential (-1.3, -1.5, and -1.7V) was applied to the bottom of the Cu needle, ground was prescribed to the far side of the electrolyte, electric insulation was applied to the remaining electrolyte sides, and an initial value of 0 V was set everywhere.

The 'Heat Transfer in Solids and Fluids' module was used to simulate the thermal field under different PTFE coverage rates. The heat transfer equation was used to estimate the thermal field in the system as a certain electric potential is applied.

$$\rho c_p u \cdot \nabla T + \nabla \cdot q = Q$$

Here, ρ is density, c_p is the specific heat capacity, u is the velocity vector (estimated to be 1.667×10^{-3} m s^{-1}), T is temperature, q is the heat flux, and Q is a heat source term (equated with the heat generated due to the applied potential). The heat flux was calculated using the following equation:

$$q = -k\nabla T$$

in which k is the thermal conductivity (401 W m^{-1} K^{-1} for Cu, 0.256 W m^{-1} K^{-1} for PTFE, and 0.599 W m^{-1} K^{-1} for the electrolyte). A reference and an initial temperature of 298 K were applied at the electrolyte and everywhere in the system, respectively.

DFT computational details. Density functional theory (DFT) calculations were performed PBE exchange-correlation functional and the projector augmented wave (PAW) method with the Vienna ab initio simulation package (VASP).[54–56] The energy cutoff of plane wave was set to 400 eV, and 2×3×1 Monkhorst-Pack *k* grids are used to Brillouin-zone integrations. The electric field (from -0.8 to 0 V•$Å^{-1}$) along the Z-axis was considered in our calculations. The convergence criteria for iteration process were the maximal residual force less than 0.02 eV•$Å^{-1}$ and the energy change less than 10^{-5} eV. We employed the climbing image nudged elastic band method to find the transition states of CO coupling. The 5×3 supercell Cu(100) surface slab was built with three layer, including 45 Cu atoms. The bottom two layer was fixed and top

layer relaxed. The vacuum layer is about 15 Å. Considering the effect of the solvent, six water molecules and one potassium atom were added near surface.

Materials. Potassium hydroxide (KOH, ACS), potassium bicarbonate ($KHCO_3$, AR, 99.5%), polyterafluoroethylene preparation (PTFE, 60 wt%), ammonium fluoride (NH_4F, AR, 98%), ammonium chloride (NH_4Cl, AR, 99.5%), sodium tetrachloroaurate(III) dihydrate ($NaAuCl_4 \cdot 2H_2O$) and sodium thiosulfate ($Na_2S_2O_3$, 99%) were purchased from Aladdin Industrial Corporation. Phosphoric acid (H_3PO_4, AR, 85%), copper sulfate ($CuSO_4 \cdot 5H_2O$, AR, 99%), citric acid ($H_3C_6H_5O_7$, AR, 99%), hydrochloric acid (HCl, GR, 38%), sulfuric acid (H_2SO_4, GR, 95~98%), hydrofluoric acid (HF, AR, ≥40%), hydrogen peroxide (H_2O_2, GR, ≥30%), sodium hydroxide (NaOH, AR, ≥96%) and sodium sulfite (Na_2SO_3, AR, ≥97%) were purchased from Sinopharm Chemical Reagent Co. Ltd. All reagents were used without further purification. Deionized water (DI) was used in the overall process of catalysts preparation and performance test.

Preparation of Cu NN and Cu-PTFE NN electrodes. Firstly, $Cu(OH)_2$ NN electrodes were prepared by an anodized method.[57] Before anodizing, the bare Cu electrode was electropolished in a two-electrode system by using 85% H_3PO_4 solution as electrolyte, Cu foil as working electrode (0.5×0.35 cm^{-2}) and platinum plate as counter electrode. A constant voltage of 4 V was applied to electropolish Cu surface for 600 s. After polishing, the electrode was flushed with deionized water several times and dried with nitrogen gas flow. The obtained glossy Cu surface was then anodized in 3 M KOH electrolyte by using polished Cu electrode as working electrode, platinum plate as counter electrode, and Ag/AgCl (3.5 M KCl) as reference electrode. A constant current of 1 mA (~5.7 mA cm^{-2}) was applied for 350 s to synthesize $Cu(OH)_2$ NNs.

Then, $Cu(OH)_2$ NNs with different PTFE coverage were prepared via a capillary percolation method. At first, several scratches on Cu substrate were constructed as channels to facilitate the transfer of PTFE solution. The PTFE solution (5 wt%, 2μL) was dropwise added at the end of scratches. PTFE solution was permeated along with the scratches and then

gradually diffused into $Cu(OH)_2$ NN arrays due to the capillary action. After complete diffusion, the excess PTFE solution was removed rapidly by dust-free paper and then dried naturally in air. The coverage rate of PTFE can be tuned by controlling the dosage of PTFE solution.

Finally, Cu NN and Cu-PTFE NN electrodes were obtained via an in-situ electrochemical reduction process. Before CO_2 electroreduction test, the as-prepared $Cu(OH)_2$ NN and $Cu(OH)_2$-PTFE NN electrodes in above were reduced under a constant potential of –1.4 V vs. RHE for at least 180 s until the current become stable.

Preparation of Cu NP. The Cu NP electrode was prepared through an electrodeposition approach. The Cu NPs were electrodeposited on Cu foil using a conventional two electrode system, Cu foil substrate was used as working electrode and graphite rod as a counter electrode. An aqueous solution of 0.1 M $CuSO_4 \cdot 5H_2O$ and 1 M citric acid was used as electrolyte. Cu NP was electrodeposited at a constant voltage of –1.5 V for 300 s. After the deposition, the samples were rinsed in distilled water and dried with nitrogen gas flow.

Materials characterization. Phases of catalysts ware characterized by using XRD (Rigaku Miniflex 600, Cu-Kα radiation with λ=1.51484Å) with a 2θ range from 5° to 80° and a scan rate of 8° min^{-1}. SEM images and EDX of the samples were obtained from a FEI Helios Nanolab 600 field emission electron microscope. TEM, HR-TEM, STEM and corresponding EDX elemental mapping images were obtained from FEI Tecnai G2 F20 field emission transmission electron microscope operated at 200 kV. XPS results were performed on Thermo Fisher Scientific-Escalab 250Xi. All the binding energies were calibrated by the C 1s peak at 284.8 eV. FTIR and in situ electrochemical ATR-FTIR measurements were performed by using Thermo iS50. The X-ray absorption spectroscopy measurements were conducted at Taiwan Beam Lines BL01C1, BL07A1, and BL17C1 at the National Synchrotron Radiation Research Center (Hsinchu, Taiwan). The concentrations of adsorbed K^+ on electrodes were detected by using Thermo Scientific ICS-600 Ion Chromatograph system. The temperature on electrode surface were measured through Infrared Thermal Camera (FLIR A615).

In situ electrochemical ATR-FTIR measurements. The in situ electrochemical ATR-FTIR measurements were performed using a Thermoelectric IR spectrometer (Thermo Fisher IS50) equipped with a liquid N_2-cooled MCT-A detector.[58,59] A customized spectro-electrochemical cell was assembled on top of a Si prism to carry out the in-situ testing process. A silicon prism crystal loading with catalysts, platinum plate and Ag/AgCl (Saturated KCl solution filling) were used as working electrode, counter electrode and reference electrode, respectively. The CO_2-saturated 0.1 M $KHCO_3$ was used as electrolyte and purged with a constant flow (20 sccm) throughout the test to enable the balance of the test environment. In this work, the catalysts that grown on Cu foil were scraped from substrate, then loaded on Au film modified Si prism by using drop-coating approach. Before catalysts loading, an Au film was deposited directly on the reflecting plane of Si prism using a chemical deposition method.[58] Firstly, Si prism was polished with a slurry of 0.5 μm Al_2O_3 and sonicated in acetone and deionized water. After polishing, the Si prism was soaked in a piranha solution (3:1 volumetric ratio of 98% H_2SO_4 and H_2O_2) for 60 min in order to clean the prism of organic contaminants. Following cleaning, the reflecting plane of Si prism was dried with nitrogen gas flow and immersed in 40% NH_4F solution for 150s to create a hydrogen-terminated surface to improve adhesion of the Au film. Then the reflecting surface was immersed in the mixture of the Au plating solution (5.75 mM $NaAuCl_4 \cdot 2H_2O$ + 0.025 M NH_4Cl + 0.075 M Na_2SO_3 + 0.025 M $Na_2S_2O_3$ + 0.026 M NaOH) and a 2 wt % HF solution (in a 4.4:1 ratio) at 55 °C for 10 min. After the deposition, the Au film was rinsed with deionized water and dried nitrogen gas flow. The catalysts (200 mg) scraped from Cu foil were dispersed in a hybrid solution included 750 μL of deionized water, 750 μL of alcohol and 100 μL of Nafion (5 wt%). Then 100 μL of catalyst ink was cast onto the Au film modified Si prism reflecting surface. FTIR spectra were obtained from an average of 32 scans with a resolution of 8 cm^{-1}, and the range of wavenumber of collected spectra was set from 1600 to 2400 cm^{-1}. Background spectrum was taken at the potential of +0.2 V vs. RHE. The spectrums depend on potential were obtained by applying single potential steps, and

collected after running 90s. The time-resolved spectrums were collected at a constant potential, and collected every 15s. Atop-bound CO (CO_L) bands are typically in the 1950–2100 cm^{-1} region. Thus, the CO peak area calculations are performed by including the area under the curve between 1950 and 2100 cm^{-1} to account for small shifts in CO peak position because of changes in coverage, dipole coupling or the impact of hydroxide adsorbed on adjacent sites.[52]

Electrochemical performance measurements. In this work, the CO_2RR performance were investigated in conventional H-cell and advanced Flow-cell. All the electrocatalytic measurements were carried out in a three-electrode system using an electrochemical station (AUT50783). All the potentials were measured against an Ag/AgCl (Saturated KCl solution filling) reference electrode and converted to RHE as follows:

$$E_{RHE} = E_{Ag/AgCl} + 0.210 + 0.059 \times pH$$

In H-cell, a Nafion-115 proton exchange membrane was used to separate sealed cell. The as-prepared electrode, Ag/AgCl (Saturated KCl solution filling) electrode, and platinum plate (2×2 cm^2) electrode were used as the working electrode, counter electrode, and reference electrode, respectively. The CO_2-saturated 0.1M $KHCO_3$ solution was used as electrolyte (pH=6.8). The cathodic compartment was continuously purged with a constant CO_2 (99.999%) flow rate (20 sccm) and vented directly into the gas-sampling loop of a GC. The electrolyte was collected and analysed by NMR after CO_2RR test (electrolysis 45 min). The ECSAs of all electrodes were estimated by double layer capacitance in CO_2-saturated 0.1 M $KHCO_3$. Non-faradaic potential ranges were selected for all samples. The cyclic voltammograms (CVs) were measured at a potential window of 0.05–0.25 V vs. RHE with different scan rates of 10, 20, 30, 40, 50, 60, 80 and 100 mV/s. The non-faradaic current density was plotted against the scan rates and the slope obtained was the double layer capacitance (C_{dl}). The roughness factor of catalysts was determined *via* C_{dl}/C_s, where C_s represents the double layer capacitance of polycrystalline Cu electrode (Cu foil). For the lead UPD, a N_2-saturated 0.1 M $HClO_4$/10 mM $Pb(ClO_4)_2$ aqueous solution was used as the electrolyte. The potential was first set at −0.35 V vs. Ag/AgCl

for 150 s and then cyclic voltammetry was recorded between −0.35 and 0 V vs. Ag/AgCl at 10 mV s^{-1}.

In Flow-cell, the PTFE membrane (pore size of 450 nm) electrode, nickel foam, and Ag/AgCl (Saturated KCl solution filling) electrode were used as the cathode, anode, and reference electrode, respectively. To prepare gas-diffusion electrode (GDE, with a size of 2 × 2 cm^2), we firstly scraped the catalysts from Cu foil, then deposited 10 mg of catalyst (mixed with 20 μL of 5 wt% Nafion in 1 ml of isopropanol) on PTFE membrane with a loading mass about 2.5 mg cm^{-2} by using an airbrush. All electrodes and the anion exchange membrane (Fumasep FAB-PK-130) were positioned and clamped together via PTFE gaskets. 20 ml of electrolyte (1 M KOH, pH=14) was circulated through both the anode and cathode chambers by two pumps with a flow rate of 10 ml min^{-1}. Meanwhile, CO_2 gas was continuously supplied to the gas chamber located at the back side of the cathode by using a mass flow controller with a flow rate of 20 ml min^{-1}. The performance of the cathodes was evaluated by performing constant-current electrolysis. The ohmic loss between the working and reference electrodes was measured using the electrochemical impedance spectroscopy technique (with a potentiostatic mode in the frequency range of 10^5 to 0.1 Hz) at the ending of the electrolysis, and 80% iR compensation (i, current; R, uncompensated resistance) was applied to correct the potentials manually.

CO_2 reduction products analysis. Gas products were analysis by GC and quantification via external standard method. Each peak in GC corresponds to a product and concentration (V) is proportional to peak area. The FEs of gas products were calculated using the equation:

$$FE = \frac{V \times Q \times P \times nF}{R \times T \times i_{total}} \times 100$$

where V is volume concentration from GC, i is current record by workstation, P is pressure, F is Faradaic constant, 96485 C mol^{-1}, R is ideal gas constant, 8.314 $m^3 \cdot Pa\ (K \cdot mol)^{-1}$, Q is flow rate, 20 mL min^{-1}, T is temperature.

Liquid products were analysis by NMR. Concentration (C_{liquid}) was obtained from NMR, V was electrolyte volume, F is Faradaic constant, Q_{total} was electricity record by workstation. The FEs of liquid products were calculated using the equation:

$$FE = \frac{C_{liquid} \times V \times nF}{Q_{total}} \times 100$$

In the flow cell, the half-cell cathode energy conversion efficiency (CEE) for ethylene and ethanol can be calculated as follows:[13,15]

$$CEE = \frac{\left(1.23 + \left(-E_{ethylene}\right)\right) \times FE_{ethylene}}{\left(1.23 + \left(-E_{applied}\right)\right)} + \frac{\left(1.23 + \left(-E_{ethanol}\right)\right) \times FE_{ethanol}}{\left(1.23 + \left(-E_{applied}\right)\right)}$$

here, the overpotential of oxygen evolution in anode is assumed to be zero. $E_{applied}$ is the measured potential values in the experiment, $FE_{ethylene}$ and $FE_{ethanol}$ are the measured Faradaic efficiency of ethylene and ethanol in percentage, $E_{ethylene}$ = 0.08 V vs. RHE and $E_{ethanol}$ = 0.09 V vs. RHE for CO_2RR.

Adsorbed K^+ measurement. The concentrations of adsorbed K^+ on electrodes were performed in 0.1M $KHCO_3$ solution by using a three-electrode system and Ion Chromatograph (IC, Thermo Scientific ICS-600). All the electrodes were run in 0.1M $KHCO_3$ solution with an applied voltage at –1.5 V vs. RHE. Once the running time reached 120 s, the electrode was directly raised above the electrolyte. Next, the electrodes were transferred with voltage and immersed in 10 ml pure water, then removed the applied potential and shaking for 1 min in pure water, to enable the adsorbed K^+ on the surface of catalysts can be completely released into the pure water. After repeating above process 10 times, the concentration of K^+ in the water was checked using an IC. The XPS of bare Cu NN and Cu-PTFE-99 NN under the conditions of before and after releasing K^+ were measured.

Electrode surface temperature measurement. The temperature on electrode surface were measured by an Infrared Thermal Camera (FLIR A615). The electrodes with an exposed area of 1×1 cm^{-2} were prepared using the same procedure as we described in previous methods. The

as-prepared electrode was connected with DC Power (Luyang, YB1731B). The temperature distribution on electrodes surface were collected under an applied constant current. We also measured the temperature on macroscopical Cu needle electrodes using the same procedure.

CO_2 and CO adsorption test. The CO_2 (or CO) adsorption on the catalysts surface were characterized by a self-designed gas adsorption electro-response device.[47] The electrodes with an exposed area of 1×1 cm^{-2} were prepared using the same procedure as we described in previous methods. The as-prepared electrode was connected with electrochemical workstation (CHI 660E) and put into a sealed container. This sealed container was connected with vacuum pump and CO_2 (or CO) alimentative system. Before CO_2 (or CO) adsorption electro-response test, the sealed container kept vacuum state by the working of vacuum pump. The curve of current as a function of time were be monitored through a multi-potential steps (0 V, –0.05 V, –0.10 V) at vacuum state, and each potential running 10s. Then CO_2 (or CO) gas was injected into the sealed container. The curve of current as a function of time were be monitored again under the same potentials and running time. Due to the adsorption of CO_2 (or CO) on catalysts surface, the current response was changed. From the difference of current density ($\Delta j = j_{gas} - j_{Vacuum}$) under the vacuum state (j_{Vacuum}) and CO_2 (or CO) atmosphere (j_{gas}), we can quantificat the adsorbed capacity of CO_2 (or CO) on catalysts surface.

Turnover frequencies (TOFs) calculations. The experimental TOFs of C_2 production on a single Cu active site were calculated by using the following equation:

$$TOF = \frac{j_{Geo} \times S}{1000 \times 12 \times n_{Cu} \times F}$$

where j_{Geo} is the geometric current density (mA cm^{-2}) of ethylene and ethanol, S is the electrode geometric area (0.175 cm^2), 12 is the number of consumed electrons for producing an ethylene (or ethanol) molecule, n_{Cu} is the mole number of surface Cu atoms (mol) and F is the Faraday constant (96485.3 C mol^{-1}). To estimate the number of active Cu atoms on catalyst surface, we proposed an approximate catalyst structure model based on SEM results.

For the single Cu NP model, the surface area of it was calculated from

$$S_{Cu\,NP} = \frac{3}{4} \times 4\pi R^2 = 3.39 \times 10^{-12}\ m^2$$

For the single Cu NN model, the surface area of it was calculated from

$$S_{Cu\,NN} = \pi r l = 9.42 \times 10^{-12}\ m^2$$

Based on the surface atomic density of Cu is C_{Cu}=1.47×10^{19} m^{-2}, the number of surface Cu atom on each Cu NP and Cu NN can be calculated as follows:

$$N_{Cu\,NP} = S_{Cu\,NP} \times C_{Cu} = 1.38 \times 10^8$$

$$N_{Cu\,NN} = S_{Cu\,NN} \times 4\pi R^2 = 4.98 \times 10^7$$

To obtain the density of nanoneedles ($D_{\text{Cu NN}}$) and nanoparticles ($D_{\text{Cu NP}}$) on electrodes, the representative SEM results were statistically analyzed, we calculated $D_{\text{Cu NN}}$=0.4772 μm^{-2}, $D_{\text{Cu NP}}$=1.0352 μm^{-2}. Based on these parameters, we can calculate the mole number of active Cu atoms on surface (n_{Cu}) using the following equation:

$$n_{Cu} = \frac{\mathrm{D} \times S \times 10^8 \times N}{N_A} \times k$$

where D is the density of nanoneedles ($D_{\text{Cu NN}}$) and nanoparticles ($D_{\text{Cu NP}}$) on electrodes, S is the electrode geometric area (0.175 cm^2), N is the number of surface Cu atoms on each Cu NN ($N_{\text{Cu NN}}$) and Cu NP ($N_{\text{Cu NP}}$), k is the correction factor of active area (obtained from ECSA) and NA is the Avogadro constant (6.02×10^{23}). For all Cu nanoneedles electrode, $D_{\text{Cu NN}}$ and $N_{\text{Cu NN}}$ is identical. For Cu NNs and Cu NPs electrodes, k=1; For Cu-PTFE-1 NNs electrode, k=0.62; For Cu-PTFE-3 NNs electrode, k=0.46; For Cu-PTFE-5 NNs electrode, k=0.37.

ASSOCIATED CONTENT

Supporting Information. The Supporting Information is available free of charge at http://pubs.acs.org. The additional theoretical calculations, characterizations, and catalytic performance results.

AUTHOR INFORMATION

Corresponding Authors

Min Liu − State Key Laboratory of Powder Metallurgy, School of Physical and Electronics, Central South University, Changsha 410083, China; Email: minliu@csu.edu.cn

Stefan A. Maier − Chair in Hybrid Nanosystems, Nanoinstitute Munich, Faculty of Physics, Ludwig-Maximilians-Universität München, D-80539 München, Germany; Department of Physics, Imperial College London, London SW7 2AZ, UK; E-mail: Stefan.Maier@physik.uni-muenchen.de

Authors

Baopeng Yang − State Key Laboratory of Powder Metallurgy, School of Physical and Electronics, Central South University, Changsha 410083, China

Kang Liu − State Key Laboratory of Powder Metallurgy, School of Physical and Electronics, Central South University, Changsha 410083, China

HuangJingWei Li − State Key Laboratory of Powder Metallurgy, School of Physical and Electronics, Central South University, Changsha 410083, China

Changxu Liu − Chair in Hybrid Nanosystems, Nanoinstitute Munich, Faculty of Physics, Ludwig-Maximilians-Universität München, D-80539 München, Germany

Junwei Fu − State Key Laboratory of Powder Metallurgy, School of Physical and Electronics, Central South University, Changsha 410083, China

Hongmei Li − State Key Laboratory of Powder Metallurgy, School of Physical and Electronics, Central South University, Changsha 410083, China

Jianan Erick Huang − Department of Electrical and Computer Engineering, University of Toronto, Toronto, Ontario M5S 1A4, Canada

Pengfei Ou − Department of Electrical and Computer Engineering, University of Toronto, Toronto, Ontario M5S 1A4, Canada

Tartela Alkayyali − Department of Mechanical and Industrial Engineering, University of Toronto, Toronto, Ontario M5S 3G8, Canada

Chao Cai − State Key Laboratory of Powder Metallurgy, School of Physical and Electronics, Central South University, Changsha 410083, China

Yuxia Duan − State Key Laboratory of Powder Metallurgy, School of Physical and Electronics, Central South University, Changsha 410083, China

Hui Liu − School of Metallurgy and Environment, Central South University, Changsha 410083, China

Pengda An − School of Materials Science and Engineering, Central South University, Changsha 410083, China

Ning Zhang − School of Materials Science and Engineering, Central South University,

Changsha 410083, China

Wenzhang Li − School of Chemistry and Chemical Engineering, Central South University, Changsha 410083, China

Xiaoqing Qiu − School of Chemistry and Chemical Engineering, Central South University, Changsha 410083, China

Chuankun Jia − College of Materials Science and Engineering, Changsha University of Science & Technology, Changsha 410114, China

Junhua Hu − School of Materials Science and Engineering, Zhengzhou University, Zhengzhou 450002, China

Liyuan Chai − School of Metallurgy and Environment, Central South University, Changsha 410083, China

Zhang Lin − School of Metallurgy and Environment, Central South University, Changsha 410083, China

Yongli Gao − Department of Physics and Astronomy, University of Rochester, Rochester, NY, 14627, USA

Miyauchi Masahiro − Department of Materials Science and Engineering, School of Materials and Chemical Technology, Tokyo Institute of Technology, Tokyo 152-8552, Japan

Emiliano Cortés − Chair in Hybrid Nanosystems, Nanoinstitute Munich, Faculty of Physics, Ludwig-Maximilians-Universität München, D-80539 München, Germany

Complete contact information is available at: https://pubs.acs.org

Author Contributions

Baopeng Yang, Kang Liu, HuangJingWei Li, and Changxu Liu contributed equally to this work.

Funding

Open access funded by Max Planck Society.

Notes

The authors declare no competing financial interest.

ACKNOWLEDGEMENTS

This work was supported by Natural Science Foundation of China (Grant No. 21872174, 22002189, 22011530423 and U1932148), Technology Cooperation Program (Grant No. 2017YFE0127800 and 2018YFE0203400), Hunan Provincial key research and development program (2020WK2002), Hunan Provincial Natural Science Foundation of China (2020JJ2041

and 2020JJ5691), Hunan Provincial Science and Technology Program (2017XK2026), Shenzhen Science and Technology Innovation Project (Grant No. JCYJ20180307151313532), National Postdoctoral Program for Innovative Talents of China, Postdoctoral Science Foundation of China (Grant No. 2018M640759), Thousand Youth Talents Plan of China and Hundred Youth Talents Program of Hunan, the Hunan Provincial Science and Technology Plan Project (Grant No. 2017TP1001), the Outstanding Youth Exchange Program of China Association for Science and Technology (Grant No.2018CASTQNJL56), and Fundamental Research Funds for the Central Universities of Central South University (2021zzts0060). We thank Prof. Edward Sargent and Dr. Joshua Wicks for helpful discussions.

REFERENCES

(1) De Luna, P.; Hahn, C.; Higgins, D.; Jaffer, S. A.; Jaramillo, T. F.; Sargent, E. H. What Would It Take for Renewably Powered Electrosynthesis to Displace Petrochemical Processes? *Science* **2019**, *364* (6438), eaav3506.

(2) Bushuyev, O. S.; De Luna, P.; Dinh, C. T.; Tao, L.; Saur, G.; van de Lagemaat, J.; Kelley, S. O.; Sargent, E. H. What Should We Make with CO_2 and How Can We Make It? *Joule* **2018**, *2* (5), 825–832.

(3) Gür, T. M. Review of Electrical Energy Storage Technologies, Materials and Systems: Challenges and Prospects for Large-Scale Grid Storage. *Energy Environ. Sci.* **2018**, *11* (10), 2696–2767.

(4) Gao, D.; Arán-Ais, R. M.; Jeon, H. S.; Roldan Cuenya, B. Rational Catalyst and Electrolyte Design for CO_2 Electroreduction towards Multicarbon Products. *Nat. Catal.* **2019**, *2* (3), 198–210.

(5) Birdja, Y. Y.; Pérez-Gallent, E.; Figueiredo, M. C.; Göttle, A. J.; Calle-Vallejo, F.; Koper, M. T. M. Advances and Challenges in Understanding the Electrocatalytic Conversion of Carbon Dioxide to Fuels. *Nat. Energy* **2019**, *4* (9), 732–745.

(6) Nitopi, S.; Bertheussen, E.; Scott, S. B.; Liu, X.; Engstfeld, A. K.; Horch, S.; Seger, B.; Stephens, I. E. L.; Chan, K.; Hahn, C.; Nørskov, J. K.; Jaramillo, T. F.; Chorkendorff, I. Progress and Perspectives of Electrochemical CO_2 Reduction on Copper in Aqueous Electrolyte. *Chem. Rev.* **2019**, *119* (12), 7610–7672.

(7) Wang, G.; Chen, J.; Ding, Y.; Cai, P.; Yi, L.; Li, Y.; Tu, C.; Hou, Y.; Wen, Z.; Dai, L. Electrocatalysis for CO_2 Conversion: From Fundamentals to Value-Added Products. *Chem. Soc. Rev.* **2021**, *50* (8), 4993–5061.

(8) Ross, M. B.; De Luna, P.; Li, Y.; Dinh, C. T.; Kim, D.; Yang, P.; Sargent, E. H. Designing Materials for Electrochemical Carbon Dioxide Recycling. *Nat. Catal.* **2019**, *2* (8), 648–658.

(9) Zhou, Y.; Che, F.; Liu, M.; Zou, C.; Liang, Z.; De Luna, P.; Yuan, H.; Li, J.; Wang, Z.; Xie, H.; Li, H.; Chen, P.; Bladt, E.; Quintero-Bermudez, R.; Sham, T. K.; Bals, S.; Hofkens, J.; Sinton, D.; Chen, G.; Sargent, E. H. Dopant-Induced Electron Localization Drives CO_2 Reduction to C_2 Hydrocarbons. *Nat. Chem.* **2018**, *10* (9), 974–980.

(10) Zhong, M.; Tran, K.; Min, Y.; Wang, C.; Wang, Z.; Dinh, C. T.; De Luna, P.; Yu, Z.; Rasouli, A. S.; Brodersen, P.; Sun, S.; Voznyy, O.; Tan, C. S.; Askerka, M.; Che, F.; Liu, M.; Seifitokaldani, A.; Pang, Y.; Lo, S. C.; Ip, A.; Ulissi, Z.; Sargent, E. H. Accelerated Discovery of CO_2 Electrocatalysts Using Active Machine Learning. *Nature* **2020**, *581* (7807), 178–183.

(11) De Luna, P.; Quintero-Bermudez, R.; DInh, C. T.; Ross, M. B.; Bushuyev, O. S.; Todorović, P.; Regier, T.; Kelley, S. O.; Yang, P.; Sargent, E. H. Catalyst Electro-Redeposition Controls Morphology and Oxidation State for Selective Carbon Dioxide Reduction. *Nat. Catal.* **2018**, *1* (2), 103–110.

(12) De Gregorio, G. L.; Burdyny, T.; Loiudice, A.; Iyengar, P.; Smith, W. A.; Buonsanti, R. Facet-Dependent Selectivity of Cu Catalysts in Electrochemical CO_2 Reduction at Commercially Viable Current Densities. *ACS Catal.* **2020**, *10* (9), 4854–4862.

(13) Wang, Y.; Wang, Z.; Dinh, C. T.; Li, J.; Ozden, A.; Golam Kibria, M.; Seifitokaldani, A.; Tan, C. S.; Gabardo, C. M.; Luo, M.; Zhou, H.; Li, F.; Lum, Y.; McCallum, C.; Xu, Y.; Liu, M.; Proppe, A.; Johnston, A.; Todorovic, P.; Zhuang, T. T.; Sinton, D.; Kelley, S. O.; Sargent, E. H. Catalyst Synthesis under CO_2 Electroreduction Favours Faceting and Promotes Renewable Fuels Electrosynthesis. *Nat. Catal.* **2020**, *3* (2), 98–106.

(14) Li, F.; Thevenon, A.; Rosas-Hernández, A.; Wang, Z.; Li, Y.; Gabardo, C. M.; Ozden, A.; Dinh, C. T.; Li, J.; Wang, Y.; Edwards, J. P.; Xu, Y.; McCallum, C.; Tao, L.; Liang, Z. Q.; Luo, M.; Wang, X.; Li, H.; O'Brien, C. P.; Tan, C. S.; Nam, D. H.; Quintero-Bermudez, R.; Zhuang, T. T.; Li, Y. C.; Han, Z.; Britt, R. D.; Sinton, D.; Agapie, T.; Peters, J. C.; Sargent, E. H. Molecular Tuning of CO_2-to-Ethylene Conversion. *Nature* **2020**, *577* (7791), 509–513.

(15) Wang, X.; Wang, Z.; García de Arquer, F. P.; Dinh, C. T.; Ozden, A.; Li, Y. C.; Nam, D. H.; Li, J.; Liu, Y. S.; Wicks, J.; Chen, Z.; Chi, M.; Chen, B.; Wang, Y.; Tam, J.; Howe, J. Y.; Proppe, A.; Todorović, P.; Li, F.; Zhuang, T. T.; Gabardo, C. M.; Kirmani, A. R.; McCallum, C.; Hung, S. F.; Lum, Y.; Luo, M.; Min, Y.; Xu, A.; O'Brien, C. P.; Stephen,

B.; Sun, B.; Ip, A. H.; Richter, L. J.; Kelley, S. O.; Sinton, D.; Sargent, E. H. Efficient Electrically Powered CO_2-to-Ethanol via Suppression of Deoxygenation. *Nat. Energy* **2020**, *5* (6), 478–486.

(16) Wang, H.; Tzeng, Y. K.; Ji, Y.; Li, Y.; Li, J.; Zheng, X.; Yang, A.; Liu, Y.; Gong, Y.; Cai, L.; Li, Y.; Zhang, X.; Chen, W.; Liu, B.; Lu, H.; Melosh, N. A.; Shen, Z. X.; Chan, K.; Tan, T.; Chu, S.; Cui, Y. Synergistic Enhancement of Electrocatalytic CO_2 Reduction to C_2 Oxygenates at Nitrogen-Doped Nanodiamonds/Cu Interface. *Nat. Nanotechnol.* **2020**, *15* (2), 131–137.

(17) Pang, Y.; Li, J.; Wang, Z.; Tan, C. S.; Hsieh, P. L.; Zhuang, T. T.; Liang, Z. Q.; Zou, C.; Wang, X.; De Luna, P.; Edwards, J. P.; Xu, Y.; Li, F.; Dinh, C. T.; Zhong, M.; Lou, Y.; Wu, D.; Chen, L. J.; Sargent, E. H.; Sinton, D. Efficient Electrocatalytic Conversion of Carbon Monoxide to Propanol Using Fragmented Copper. *Nat. Catal.* **2019**, *2* (3), 251–258.

(18) Liu, M.; Liu, M.; Wang, X.; Kozlov, S. M.; Cao, Z.; De Luna, P.; Li, H.; Qiu, X.; Liu, K.; Hu, J.; Jia, C.; Wang, P.; Zhou, H.; He, J.; Zhong, M.; Lan, X.; Zhou, Y.; Wang, Z.; Li, J.; Seifitokaldani, A.; Dinh, C. T.; Liang, H.; Zou, C.; Zhang, D.; Yang, Y.; Chan, T. S.; Han, Y.; Cavallo, L.; Sham, T. K.; Hwang, B. J.; Sargent, E. H. Quantum-Dot-Derived Catalysts for CO_2 Reduction Reaction. *Joule* **2019**, *3* (7), 1703–1718.

(19) Zhuang, T. T.; Liang, Z. Q.; Seifitokaldani, A.; Li, Y.; De Luna, P.; Burdyny, T.; Che, F.; Meng, F.; Min, Y.; Quintero-Bermudez, R.; Dinh, C. T.; Pang, Y.; Zhong, M.; Zhang, B.; Li, J.; Chen, P. N.; Zheng, X. L.; Liang, H.; Ge, W. N.; Ye, B. J.; Sinton, D.; Yu, S. H.; Sargent, E. H. Steering Post-C-C Coupling Selectivity Enables High Efficiency Electroreduction of Carbon Dioxide to Multi-Carbon Alcohols. *Nat. Catal.* **2018**, *1* (6), 421–428.

(20) Liu, M.; Pang, Y.; Zhang, B.; De Luna, P.; Voznyy, O.; Xu, J.; Zheng, X.; Dinh, C. T.; Fan, F.; Cao, C.; de Arquer, F. P. G.; Safaei, T. S.; Mepham, A.; Klinkova, A.; Kumacheva, E.; Filleter, T.; Sinton, D.; Kelley, S. O.; Sargent, E. H. Enhanced Electrocatalytic CO_2 Reduction via Field-Induced Reagent Concentration. *Nature* **2016**, *537* (7620), 382–386.

(21) Chen, L. D.; Urushihara, M.; Chan, K.; Nørskov, J. K. Electric Field Effects in Electrochemical CO_2 Reduction. *ACS Catal.* **2016**, *6* (10), 7133–7139.

(22) Che, F.; Gray, J. T.; Ha, S.; Kruse, N.; Scott, S. L.; McEwen, J.-S. Elucidating the Roles of Electric Fields in Catalysis: A Perspective. *ACS Catal.* **2018**, *8* (6), 5153–5174.

(23) Liu, P.; Chen, B.; Liang, C.; Yao, W.; Cui, Y.; Hu, S.; Zou, P.; Zhang, H.; Fan, H. J.; Yang, C. Tip-Enhanced Electric Field: A New Mechanism Promoting Mass Transfer in Oxygen Evolution Reactions. *Adv. Mater.* **2021**, *33* (9), 1–9.

(24) Gao, F.; Hu, S.; Zhang, X.; Zheng, Y.; Wang, H.; Niu, Z.; Yang, P.; Bao, R.; Ma, T.; Dang, Z.; Guan, Y.; Zheng, X.; Zheng, X.; Zhu, J.; Gao, M.; Yu, S. High- Curvature Transition- Metal Chalcogenide Nanostructures with a Pronounced Proximity Effect Enable Fast and Selective CO_2 Electroreduction. *Angew. Chem., Int. Ed.* **2020**, *132* (22), 8784–8790.

(25) Nairan, A.; Liang, C.; Chiang, S.-W.; Wu, Y.; Zou, P.; Khan, U.; Liu, W.; Kang, F.; Guo, S.; Wu, J.; Yang, C. Proton Selective Adsorption on Pt–Ni Nano-Thorn Array Electrodes for Superior Hydrogen Evolution Activity. *Energy Environ. Sci.* **2021**, *14* (3), 1594–1601.

(26) Jiang, H.; Hou, Z.; Luo, Y. Unraveling the Mechanism for the Sharp-Tip Enhanced Electrocatalytic Carbon Dioxide Reduction: The Kinetics Decide. *Angew. Chem., Int. Ed.* **2017**, *56* (49), 15617–15621.

(27) Shetty, M.; Ardagh, M. A.; Pang, Y.; Abdelrahman, O. A.; Dauenhauer, P. J. Electric-Field-Assisted Modulation of Surface Thermochemistry. *ACS Catal.* **2020**, *10* (21), 12867–12880.

(28) Robatjazi, H.; Zhao, H.; Swearer, D. F.; Hogan, N. J.; Zhou, L.; Alabastri, A.; McClain, M. J.; Nordlander, P.; Halas, N. J. Plasmon-Induced Selective Carbon Dioxide Conversion on Earth-Abundant Aluminum-Cuprous Oxide Antenna-Reactor Nanoparticles. *Nat. Commun.* **2017**, *8* (1), 27.

(29) Zhang, X.; Li, X.; Zhang, D.; Su, N. Q.; Yang, W.; Everitt, H. O.; Liu, J. Product Selectivity in Plasmonic Photocatalysis for Carbon Dioxide Hydrogenation. *Nat. Commun.* **2017**, *8* (1), 14542.

(30) Chen, Y.; DeGlee, B.; Tang, Y.; Wang, Z.; Zhao, B.; Wei, Y.; Zhang, L.; Yoo, S.; Pei, K.; Kim, J. H.; Ding, Y.; Hu, P.; Tao, F. F.; Liu, M. A Robust Fuel Cell Operated on Nearly Dry Methane at 500°C Enabled by Synergistic Thermal Catalysis and Electrocatalysis. *Nat. Energy* **2018**, *3* (12), 1042–1050.

(31) Niether, C.; Faure, S.; Bordet, A.; Deseure, J.; Chatenet, M.; Carrey, J.; Chaudret, B.; Rouet, A. Improved Water Electrolysis Using Magnetic Heating of FeC–Ni Core–Shell Nanoparticles. *Nat. Energy* **2018**, *3* (6), 476–483.

(32) Zhou, S.; Yang, X.; Xu, X.; Dou, S. X.; Du, Y.; Zhao, J. Boron Nitride Nanotubes for Ammonia Synthesis: Activation by Filling Transition Metals. *J. Am. Chem. Soc.* **2020**, *142* (1), 308–317.

(33) Clark, E. L.; Ringe, S.; Tang, M.; Walton, A.; Hahn, C.; Jaramillo, T. F.; Chan, K.; Bell, A. T. Influence of Atomic Surface Structure on the Activity of Ag for the Electrochemical Reduction of CO_2 to CO. *ACS Catal.* **2019**, *9* (5), 4006–4014.

(34) Hartschuh, A. Tip-Enhanced near-Field Optical Microscopy. *Angew. Chem., Int. Ed.* **2008**, *47* (43), 8178–8191.

(35) D'Agosta, R.; Sai, N.; Di Ventra, M. Local Electron Heating in Nanoscale Conductors. *Nano Lett.* **2006**, *6* (12), 2935–2938.

(36) Downes, A.; Salter, D.; Elfick, A. Heating Effects in Tip-Enhanced Optical Microscopy. *Opt. Express* **2006**, *14* (12), 5216.

(37) Jin, C. Y.; Li, Z.; Williams, R. S.; Lee, K. C.; Park, I. Localized Temperature and Chemical Reaction Control in Nanoscale Space by Nanowire Array. *Nano Lett.* **2011**, *11* (11), 4818–4825.

(38) Kortlever, R.; Shen, J.; Schouten, K. J. P.; Calle-Vallejo, F.; Koper, M. T. M. Catalysts and Reaction Pathways for the Electrochemical Reduction of Carbon Dioxide. *J. Phys. Chem. Lett.* **2015**, *6* (20), 4073–4082.

(39) Todorova, T. K.; Schreiber, M. W.; Fontecave, M. Mechanistic Understanding of CO_2 Reduction Reaction (CO_2RR) Toward Multicarbon Products by Heterogeneous Copper-Based Catalysts. *ACS Catal.* **2020**, *10* (3), 1754–1768.

(40) Bagger, A.; Ju, W.; Varela, A. S.; Strasser, P.; Rossmeisl, J. Electrochemical CO_2 Reduction: Classifying Cu Facets. *ACS Catal.* **2019**, *9* (9), 7894–7899.

(41) Iyengar, P.; Kolb, M. J.; Pankhurst, J. R.; Calle-Vallejo, F.; Buonsanti, R. Elucidating the Facet-Dependent Selectivity for CO_2 Electroreduction to Ethanol of Cu-Ag Tandem Catalysts. *ACS Catal.* **2021**, *11* (8), 4456–4463.

(42) Charnay, B. P.; Cui, Z.; Marx, M. A.; Palazzo, J.; Co, A. C. Insights into the CO_2 Reduction Pathway through the Electrolysis of Aldehydes on Copper. *ACS Catal.* **2021**, *11* (7), 3867–3876.

(43) Montoya, J. H.; Shi, C.; Chan, K.; Nørskov, J. K. Theoretical Insights into a CO Dimerization Mechanism in CO_2 Electroreduction. *J. Phys. Chem. Lett.* **2015**, *6* (11), 2032–2037.

(44) Liu, C.; Qian, J.; Ye, Y.; Zhou, H.; Sun, C. J.; Sheehan, C.; Zhang, Z.; Wan, G.; Liu, Y. S.; Guo, J.; Li, S.; Shin, H.; Hwang, S.; Gunnoe, T. B.; Goddard, W. A.; Zhang, S.

Oxygen Evolution Reaction over Catalytic Single-Site Co in a Well-Defined Brookite TiO_2 Nanorod Surface. *Nat. Catal.* **2021**, *4* (1), 36–45.

(45) An, P.; Wei, L.; Li, H.; Yang, B.; Liu, K.; Fu, J.; Li, H.; Liu, H.; Hu, J.; Lu, Y.-R.; Pan, H.; Chan, T.-S.; Zhang, N.; Liu, M. Enhancing CO_2 Reduction by Suppressing Hydrogen Evolution with Polytetrafluoroethylene Protected Copper Nanoneedles. *J. Mater. Chem. A* **2020**, *8* (31), 15936–15941.

(46) Zhuang, T. T.; Pang, Y.; Liang, Z. Q.; Wang, Z.; Li, Y.; Tan, C. S.; Li, J.; Dinh, C. T.; De Luna, P.; Hsieh, P. L.; Burdyny, T.; Li, H. H.; Liu, M.; Wang, Y.; Li, F.; Proppe, A.; Johnston, A.; Nam, D. H.; Wu, Z. Y.; Zheng, Y. R.; Ip, A. H.; Tan, H.; Chen, L. J.; Yu, S. H.; Kelley, S. O.; Sinton, D.; Sargent, E. H. Copper Nanocavities Confine Intermediates for Efficient Electrosynthesis of C_3 Alcohol Fuels from Carbon Monoxide. *Nat. Catal.* **2018**, *1* (12), 946–951.

(47) Chen, K.; Liu, K.; An, P.; Li, H.; Lin, Y.; Hu, J.; Jia, C.; Fu, J.; Li, H.; Liu, H.; Lin, Z.; Li, W.; Li, J.; Lu, Y. R.; Chan, T. S.; Zhang, N.; Liu, M. Iron Phthalocyanine with Coordination Induced Electronic Localization to Boost Oxygen Reduction Reaction. *Nat. Commun.* **2020**, *11* (1), 1–8.

(48) Malkani, A. S.; Li, J.; Anibal, J.; Lu, Q.; Xu, B. Impact of Forced Convection on Spectroscopic Observations of the Electrochemical CO Reduction Reaction. *ACS Catal.* **2020**, *10* (2), 941–946.

(49) Wuttig, A.; Liu, C.; Peng, Q.; Yaguchi, M.; Hendon, C. H.; Motobayashi, K.; Ye, S.; Osawa, M.; Surendranath, Y. Tracking a Common Surface-Bound Intermediate during CO_2-to-Fuels Catalysis. *ACS Cent. Sci.* **2016**, *2* (8), 522–528.

(50) Katayama, Y.; Nattino, F.; Giordano, L.; Hwang, J.; Rao, R. R.; Andreussi, O.; Marzari, N.; Shao-Horn, Y. An in Situ Surface-Enhanced Infrared Absorption Spectroscopy Study of Electrochemical CO_2 Reduction: Selectivity Dependence on Surface C-Bound and O-Bound Reaction Intermediates. *J. Phys. Chem. C* **2019**, *123* (10), 5951–5963.

(51) Li, H.; Qin, X.; Jiang, T.; Ma, X.; Jiang, K.; Cai, W. Changing the Product Selectivity for Electrocatalysis of CO_2 Reduction Reaction on Plated Cu Electrodes. *ChemCatChem* **2019**, *11* (24), 6139–6146.

(52) Heyes, J.; Dunwell, M.; Xu, B. CO_2 Reduction on Cu at Low Overpotentials with Surface-Enhanced in Situ Spectroscopy. *J. Phys. Chem. C* **2016**, *120* (31), 17334–17341.

(53) Borguet, E.; Dai, H. L. Site-Specific Properties and Dynamical Dipole Coupling of CO Molecules Adsorbed on a Vicinal Cu(100) Surface. *J. Chem. Phys.* **1994**, *101* (10), 9080–9095.

(54) Kresse, G.; Hafner, J. Ab Initio Molecular-Dynamics Simulation of the Liquid-Metal–Amorphous-Semiconductor Transition in Germanium. *Phys. Rev. B* **1994**, *49* (20), 14251–14269.

(55) Blöchl, P. E. Projector Augmented-Wave Method. *Phys. Rev. B* **1994**, *50* (24), 17953–17979.

(56) Perdew, J. P.; Burke, K.; Ernzerhof, M. Generalized Gradient Approximation Made Simple. *Phys. Rev. Lett.* **1996**, *77* (18), 3865–3868.

(57) Lee, S. Y.; Jung, H.; Kim, N.-K.; Oh, H.-S.; Min, B. K.; Hwang, Y. J. Mixed Copper States in Anodized Cu Electrocatalyst for Stable and Selective Ethylene Production from CO_2 Reduction. *J. Am. Chem. Soc.* **2018**, *140* (28), 8681–8689.

(58) Zhu, S.; Jiang, B.; Cai, W.-B.; Shao, M. Direct Observation on Reaction Intermediates and the Role of Bicarbonate Anions in CO_2 Electrochemical Reduction Reaction on Cu Surfaces. *J. Am. Chem. Soc.* **2017**, *139* (44), 15664–15667.

(59) Zhang, H.; Chang, X.; Chen, J. G.; Goddard, W. A.; Xu, B.; Cheng, M.-J.; Lu, Q. Computational and Experimental Demonstrations of One-Pot Tandem Catalysis for Electrochemical Carbon Dioxide Reduction to Methane. *Nat. Commun.* **2019**, *10* (1), 3340.

TOC Graphic

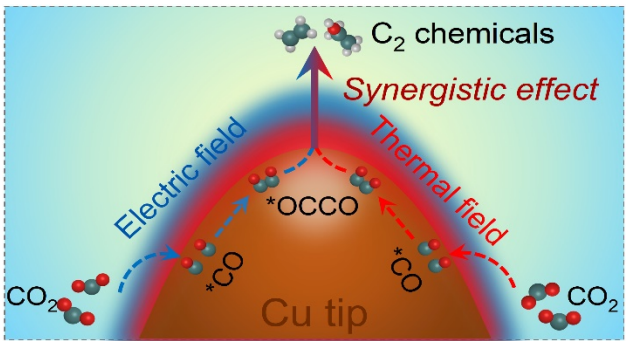
C2 chemicals
Synergistic effect
Electric field
Thermal field
*OCCO
*CO
*CO
CO2
CO2
Cu tip